Editors' Suggestion

Quasiparticle and excitonic properties of monolayer $1T'$ WTe_2 within many-body perturbation theory

Jinyuan Wu [1], Bowen Hou,[1] Wenxin Li [2], Yu He [2] and Diana Y. Qiu [1,*]

[1]*Department of Mechanical Engineering and Materials Science, Yale University, New Haven, Connecticut 06520, USA*

[2]*Department of Applied Physics, Yale University, New Haven, Connecticut 06511, USA*

(Received 17 May 2024; revised 25 July 2024; accepted 29 July 2024; published 16 August 2024)

In the monolayer limit, $1T'$ WTe_2 is a two-dimensional topological insulator exhibiting the quantum spin Hall effect and is believed to host an excitonic insulator ground state. However, theoretical analysis of this system is complicated by the difficulty of obtaining descriptions of the single-quasiparticle band structure consistent with experimental measurement within conventional first-principles techniques. Previous band-structure calculations using the Perdew-Burke-Ernzerhof functional and a one-shot *GW* approximation result in a semimetallic band structure, while calculations with hybrid functionals appear to open a band gap. Here, we demonstrate that self-consistently updating wave functions within a static *GW* approximation (static COHSEX) can reproduce the insulating band structure experimentally observed by angle-resolved photoemission spectroscopy without resorting to mechanisms beyond the quasiparticle picture. Finally, a finite-momentum Bethe-Salpeter equation calculation on top of self-consistent *GW* results in negative exciton excitation energies, leaving open the possibility of excitonic instability in $1T'$ monolayer WTe_2.

DOI: 10.1103/PhysRevB.110.075133

I. INTRODUCTION

The transition-metal dichalcogenide (TMD) WTe_2 is known to host exotic electronic states in both bulk and monolayer forms [1–11]. For instance, the strong spin-orbit coupling (SOC) in $1T'$ monolayer WTe_2 causes band inversion and turns the system into a topological insulator with quantum spin Hall edge states. The corresponding insulating bulk electron bands and conducting topological boundary states have been observed in scanning tunneling spectroscopy (STS), angle-resolved photoemission spectroscopy (ARPES), scanning tunneling microscopy (STM), conductance measurements, and microwave impedance microscopy (MIM) [5–8]. Apart from its topological properties, $1T'$ monolayer WTe_2 also hosts metal-like quantum oscillations and a Hall effect, indicating that an abundance of carriers exist in the ground state, and hence it is likely that the material is not a band insulator and the observed bulk band gap arises from a correlated ground state [9,10]. The possibility of a correlated ground state was further demonstrated by the fact that the conductance rapidly falls as the temperature drops below 100 K, and doping in the low-conductance region does not immediately improve conductivity, which can be evidence of a semimetal-correlated insulator phase transition [11]. Additionally, first-principles Bethe-Salpeter equation (BSE) calculations of excitons in monolayer $1T'$ WTe_2 [11] reveal negative exciton excitation energies, hinting at the possibility that it may host an excitonic insulator ground state, a BCS- or BEC-like state [12–14] where excitons condense due to instability of the band insulator ground state [15–18]. Such excitonic insulator ground states have also been proposed in several other systems according to evidence from band renormalization observed in ARPES spectra [19], exciton compressibility without charge compressibility [20], enhanced Coulomb drag effects [21], enhanced electroluminescence with abnormal photon statistics together with tunneling proportional to the density of electron-hole pairs [22], and negative exciton frequencies observed in *ab initio* many-body perturbation theory (MBPT) calculations [23–26].

Theoretical analysis of monolayer $1T'$ WTe_2 is complicated by the fact that most widely used first-principles methods are designed to study weakly to moderately correlated metals and band insulators, where conventional band theory holds. Within such first-principles methods, negative exciton excitation energies calculated using the MBPT *GW* plus Bethe-Salpeter equation (*GW*-BSE) approach [27–32] are frequently interpreted as indirect evidence of the possibility of an excitonic insulator ground state [23–26]. The *GW*-BSE calculation is commonly performed as a one-shot correction on top of a ground state obtained from density functional theory (DFT) [33–37]. However, results from such an approach can be challenging to interpret and depend sensitively on the initial independent-particle ground state and band structure. If the initial independent-particle state is metallic, identification of negative excitation energy states is numerically ambiguous, while an initial insulating quasiparticle (QP) gap raises the question of whether the experimentally observed gap is actually driven by an excitonic instability or could be opened through other means, like structural relaxation or single-quasiparticle renormalization within MBPT. In the case of monolayer $1T'$ WTe_2, starting from the generalized gradient approximation of Perdew, Burke, and Ernzerhof (PBE) [38] results in a gapless semimetallic

*Contact author: diana.qiu@yale.edu

ground state [39–41]. A one-shot G_0W_0 correction, which is expected to correct the inherent underestimation of the band gap by conventional DFT [28,42], is unable to open the gap [43]. The Heyd-Scuseria-Ernzerhof (HSE) hybrid functional [44], which contains a fraction of the exact exchange, directly gives a gapped band structure for monolayer $1T'$ WTe_2 [5,39,45–48]. Intriguingly, the HSE band structure already agrees well with ARPES measurements [5], raising the question of whether the ARPES measurements are of the correlated state or a band insulator state. Answering these questions requires understanding the root cause of the disagreement between band structures predicted in HSE and one-shot *GW*, which are usually expected to be comparable [49].

BSE calculations on top of the HSE band structure result in negative energy excitons [11], suggesting a possible excitonic insulator ground state. However, one theoretical caveat is that the electron-hole interaction within BSE is the variational derivative of the single-quasiparticle *GW* self-energy [30,50]. Thus, to treat all interactions consistently, BSE calculations should be done on top of a *GW* band structure [24–26]. Previous BSE calculations predicting negative exciton excitation energies [11] perform BSE calculations directly on an HSE band structure (BSE@HSE). Thus, there remain open questions about the correct independent-quasiparticle starting point for BSE calculations on monolayer $1T'$ WTe_2, the conditions under which a gap can be opened at the independent QP level, and the conditions under which negative energy excitons may be found.

This paper is a systematic investigation of the validity of the conventional *GW*-BSE methodology in monolayer $1T'$ WTe_2, and the conditions under which an exciton instability can be observed. At the single QP level, we start by exploring three factors that could potentially open a band gap without resorting to semiempirical hybrid functionals: the convergence of the cutoff parameters [51], strain and relaxation of the crystal structure, and the self-consistency of the wave functions within *GW* [42,52]. We find that self-consistently updating the QP wave functions with both the static *GW* approximation (i.e., static-COHSEX) [27,28,53] and frequency-dependent *GW* self-energy produces a gapped band structure that agrees qualitatively with previous ARPES measurements [5]. A uniaxial, out-of-plane compressive strain or equivalently a biaxial, in-plane tensile strain can also open the band gap, but the shape of the valence bands is distorted compared to ARPES [5]. For the BSE part, we find that BSE predicts negative exciton excitation energies when starting from a one-shot G_0W_0 calculation on top of wave functions obtained within self-consistent static-COHSEX (G_0W_0@scCOHSEX), consistent with previous BSE@HSE results [11]. Therefore, a correlated ground state due to exciton instability is likely.

This paper is organized as follows. In Sec. II, we outline details of the first-principles *GW*-BSE methodologies employed in this paper; Sec. III discusses the influence of the structural starting point on DFT and *GW* quasiparticle energies; Sec. IV focuses on the role of self-consistency in *GW*; Sec. V explores the possibility of exciton instability in monolayer $1T'$ WTe_2. We conclude in Sec. VI.

II. COMPUTATIONAL DETAILS

We start by performing PBE calculations as implemented in the QUANTUM ESPRESSO (QE) software package [54,55]. Fully relativistic Optimized Norm-Conserving Vanderbilt (ONCV) SG15 PBE pseudopotentials [56–58] and a noncollinear spinor formalism are used to capture strong SOC effects in $1T'$ monolayer WTe_2 [5]. The self-consistent field calculation is performed on a $40 \times 40 \times 1$ Monkhorst-Pack **k**-grid with a cutoff of 80 Ry for the plane-wave components of the wave function. We use Wannier interpolation via the WANNIER90 package [59–62] and the `inteqp` utility provided by the BerkeleyGW (BGW) software package [63] to plot the band structures. Calculations of the projected density of states use PSLibrary pseudopotentials [64], which carry atomic wave-function information.

GW and *GW*-BSE calculations are performed with the BerkeleyGW software package [63]. The *GW* calculation is performed on a uniform $20 \times 20 \times 1$ **k**-grid, and the frequency dependence is included through the Hybertsen-Louie generalized plasmon pole model (HL-GPP) [28]. Spinor wave functions are used to capture the strong SOC effects [65,66]. The Coulomb interaction is truncated to prevent unphysical interaction between periodic images of the monolayer [67]. Plane-wave components up to 30 Ry are included in the evaluation of the dielectric matrix, and 4000 bands are included in the sum over bands in the calculation of the polarizability and *GW* self-energy, which is sufficient to converge the direct band gap within $\sim$0.001 eV at the four corners of the irreducible first Brillouin zone [Fig. 1(b)]. Stochastic pseudobands are used to replace high-energy conduction bands above a protection window of 4.0 Ry to speed up the calculation of the sum over empty states in the polarizability and self-energy [51,68–70]. To explore the effect of strain, calculations are performed on both relaxed and strained structures.

Additionally, to explore the effect of the mean-field starting point, we self-consistently update the QP wave functions by rediagonalizing the single-particle Hamiltonian with the *GW* self-energy matrix. We refer to this procedure as nondiagonal self-consistent G_0W_0 (scG_0W_0). Due to computational cost, self-consistency with the *GW* self-energy is only evaluated for the k-points at the band edge. In the full Brillouin zone, we update the QP wave functions using self-consistent *GW* in the static limit, i.e., the static Coulomb-hole screened exchange (static COHSEX) approximation [27,28,53]. Then, we perform a one-shot G_0W_0 calculation on top of the self-consistent static-COHSEX wave functions. We refer to this procedure as G_0W_0@scCOHSEX.

Finally, we explore the possibility of exciton instability by calculating the exciton excitation energy within *GW*-BSE for both the lowest-energy direct exciton and lowest-energy finite momentum exciton [71] commensurate with our **k**-grid. Excitonic instability appears when the exciton excitation energy is negative, or equivalently when the exciton binding energy exceeds the (direct or indirect) band gap. BSE calculations are performed on top of *GW* band structures and two different types of wave functions: PBE wave functions strained to open a gap, and QP wave functions calculated within scCOHSEX [27,28,53]. The BSE kernel is evaluated on a $20 \times 20 \times 1$

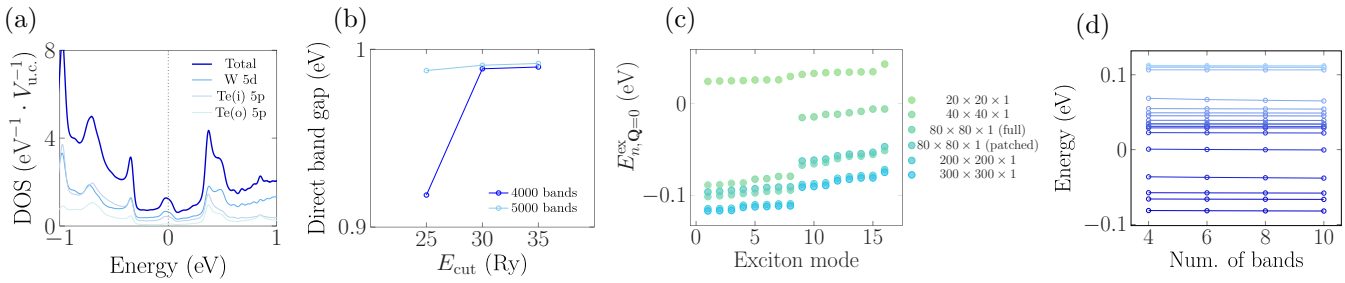

FIG. 1. Computational details. (a) Density of states (DOS) of monolayer $1T'$ WTe_2 with the crystal structure in Ref. [43], where Te(i) refers to the two Te atoms that are close to the W atoms, and the label Te(o) refers to other Te atoms. (b) Direct band gap at Γ point vs the number of bands and the cutoff energy in G_0W_0 calculation. The change of the direct band gap is on the order of meV after the number of bands reaches 4000 and the cutoff energy reaches 30 Ry. These cutoff parameters are then used in the following *GW* calculations. (c) Excitation energies of the first 16 $\mathbf{Q} = \mathbf{0}$ excitons vs the density of the fine **k**-grid in the BSE@3%-strained PBE calculation in Sec. V. The coarse **k**-grid is kept to 20 × 20 × 1. The 200 × 200 × 1 and 300 × 300 × 1 grids are calculated on a patch in the Brillouin zone. Convergence is reached at 200 × 200 × 1. (d) Convergence of the energies of the first 20 exciton states in the BSE@G_0W_0@scCOHSEX calculation in Sec. V with respect to the number of conduction bands and valence bands, which are set to be equal to each other, included in the BSE Hamiltonian. Convergence is achieved when four conduction bands and four valence bands are included.

coarse **k**-grid. For the PBE wave functions, the BSE kernel is then interpolated onto a 200 × 200 × 1 fine **k**-grid using a patched dual grid interpolation scheme [30,72–76]. To reduce the computational cost, the fine grid used is not the full Monkhorst-Pack grid but two patches of radius 0.1 in fractional coordinates centered on the two conduction-band valleys where the direct band gap is the smallest [Fig. 2(d)]. For the calculation with the QP wave functions from scCOHSEX, the self-consistency is too computationally expensive to perform on a fine **k**-grid. Hence, the BSE calculation is performed without interpolation on the coarse 20 × 20 × 1 **k**-grid. The results of the BSE@G_0W_0@scCOHSEX calculation should be compared with the calculation on the PBE wave functions to extrapolate changes in the exciton energies with *k*-point convergence [Fig. 1(c)]. In the BSE@G_0W_0@scCOHSEX calculation the dielectric matrix is recalculated from the insulating G_0W_0@scCOHSEX band structure. Convergence over the number of conduction bands and valence bands in the BSE calculation is relatively easy because the lowest-energy excitons are primarily composed of the highest two valence bands and the lowest two conduction bands, and therefore as few as four conduction bands and four valence bands are sufficient for good convergence of the first 10 exciton states [Fig. 1(d)]. The BSE kernel on the coarse 20 × 20 × 1 grid in all three cases in Sec. V is calculated using 10 conduction bands and 10 valence bands. When interpolation to the 200 × 200 × 1 **k**-grid is performed, four conduction bands and six valence bands are kept in the interpolated BSE kernel.

III. INFLUENCE OF THE STRUCTURAL STARTING POINT ON THE QUASIPARTICLE BAND STRUCTURE

We start by analyzing the band structure calculated at the PBE level and the G_0W_0 level starting from (1) the structure relaxed with the PBE functional with the lattice parameters reported in Ref. [43], and (2) a series of structures with a uniaxial out-of-plane compressive strain, where the in-plane lattice parameter is relaxed or kept fixed. The PBE and *GW*@PBE band structures are shown in Fig. 2. In our analysis, we will focus on two main features of the band structure: (1) $E_{c1} - E_{v1}$, the indirect band gap or the overlap of the highest valence band and the lowest conduction band, and (2) $E_{v1} - E_{v2}$, the energy difference between the two highest valence bands [Fig. 2(b)]. These quantities are summarized in Table I for the relaxed structure and the 3%-strained structure, which exhibits a band gap with magnitude comparable to the experimental band gap at the PBE level.

The PBE and G_0W_0@PBE band structures for the relaxed structure are shown in Fig. 2(c). We observe a larger G_0W_0 correction than the one in Ref. [43], which we attribute to the larger cutoff parameters we use and the crystal structure difference. In fact, the G_0W_0 correction in Ref. [43] is negative, which we also observe in underconverged scG_0W_0, indicating that the sign of the *GW* correction is highly sensitive to convergence parameters. However, consistent with Ref. [43], we find a negative band gap at both the PBE and G_0W_0@PBE level, so the G_0W_0 correction is still insufficient to open a band gap.

In Ref. [43], strain is invoked to explain the contradiction between the semimetallic G_0W_0 band structure and the experimentally observed bulk band gap. Reference [43] demonstrates that a 2 % biaxial tensile strain opens a band gap within PBE. In this work, we show that a compressive uniaxial strain in the *c* direction is also able to open the band gap [Fig. 2(e)]. Out-of-plane compressive strain combined with in-plane relaxation always leads to a larger band gap. If the strain is introduced without in-plane relaxation, the strain threshold for the semimetal-insulator transition is ∼5 %. However, if we relax the structure in the *xy* plane after introducing a strain in the *c* direction, the band gap increases and a gap is opened at ∼1.5 % strain. The relation between the out-of-plane strain along the *c*-axis and the induced in-plane strain is approximately linear, and the corresponding in-plane strain at the semimetal-insulator transition is ∼0.45 %, which is smaller than previously reported values of ∼2 % [43]. We note that in Ref. [5], the experimentally measured lattice constant *a* is 6.3(2) Å, and the two publicly available crystal structures in Ref. [43] (from DFT relaxation) and Ref. [47] (from the bulk data [78]) and the eight relaxed structures in

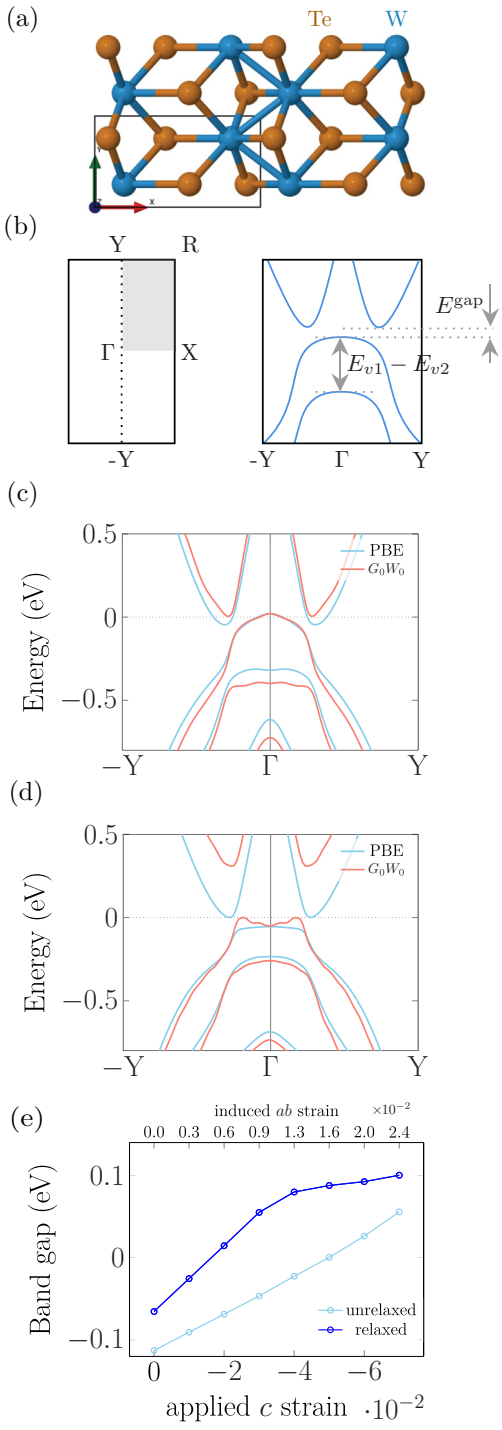

FIG. 2. PBE and G_0W_0@PBE calculations of the electronic band structure. (a) The crystal structure. (b) The first Brillouin zone and a schematic of the band structure with key energy differences labeled; the gray part is the irreducible Brillouin zone. (c), (d) The band structure along the Γ-*Y* path based on the structure relaxed directly from the structure reported in Ref. [43] (c) and with a 3% compressive out-of-plane strain (d). The zero-energy point of both PBE and G_0W_0@PBE bands is fixed to the Fermi energy of the PBE calculation to enable easier visual comparison of the bands. (e) Relation between the band gap, the compressive strain in the *c*-direction, and the tensile strain in the *ab* plane induced by the *c*-direction uniaxial strain.

Fig. 2(e), which may be semimetallic or insulating, all lie in this range. The lattice constants of our unstrained, relaxed crystal structure are $a = 6.34$ Å, $b = 3.52$ Å.

Given the strong influence of crystal structure on the qualitative properties of the electronic structure, and the possibility that the experimentally measured sample is naturally strained, it is possible that the $1T'$ WTe_2 monolayer observed in experiments has a band gap opened due to strain [43,48]. To explore this possibility, we apply a 3% out-of-plane, uniaxial strain to the crystal structure, inducing a 62 meV indirect band gap on the $20 \times 20 \times 1$ grid, which is reduced to 0.055 eV after interpolation to a dense **k**-path (Table I) and roughly agrees with the experimentally measured indirect band gap of 55(20) meV [5]. With this level of strain, the distance between the two highest valence bands and the two second highest valence bands is severely underestimated and is only half of the ∼0.5 eV experimentally observed value [Table I, Fig. 2(d)]. After a G_0W_0 correction is added on top of the PBE band energies, the indirect band gap increases to 308 meV, and the valence band develops a camelback shape, which is inconsistent with experimental measurements. We attribute this large renormalization to the reduced screening coming from the insulating starting point. Because we are unable to obtain the realistic band gap and the $E_{v1} - E_{v2}$ at the same time, regardless of the computational scheme used, we conclude that straining the structure alone is unlikely to account for the band gap seen in ARPES [5].

IV. QUASIPARTICLE WAVE FUNCTIONS AND SELF-CONSISTENCY

Next, we analyze the effect of updating the QP wave functions at the *GW* level. Figure 3(a) displays the overlap between the initial PBE wave functions and the wave functions after rediagonalizing with the G_0W_0 self-energy. The overlaps are dominated by a 2×2 block structure [highlighted by gray boxes in Fig. 3(a)] along the diagonal corresponding to the spin degenerate spaces. However, there is also significant coupling between these blocks, indicating substantial changes to the wave functions. Rediagonalizing the *GW* self-energy on the $20 \times 20 \times 1$ **k**-grid opens the indirect band gap to 7 meV (Table I). We note that due to the computational cost, performing a full update of the quasiparticle wave functions at all relevant **k**-points is not tractable, and this 7 meV indirect band gap is the gap between the highest valence-band energy at Γ and the lowest conduction-band energy at $\mathbf{k} = (0, 0.15, 0)$ on the $20 \times 20 \times 1$ grid, which does not contain the *k*-point corresponding to the conduction-band minimum. The true scG_0W_0 indirect band gap is likely slightly smaller.

As a computationally cheaper alternative to scG_0W_0, self-consistent static-COHSEX is performed to update the wave functions, and a one-shot G_0W_0 is then performed on top of the static-COHSEX wave functions. The band structure is shown in Fig. 3(b). This procedure results in a 52 meV band gap on the $20 \times 20 \times 1$ grid, which is surprisingly close to the 55(20) meV experimental observation and the HSE calculation in Ref. [5]. We note again that the reported gap corresponds to the smallest gap on the $20 \times 20 \times 1$ **k**-grid. The actual conduction-band minimum is not in the **k**-grid, so the actual indirect band gap is slightly smaller than the

TABLE I. Indirect band gaps and distances between the highest valence bands and the second highest valence bands measured by ARPES and predicted by PBE and *GW*@PBE. The scG_0W_0 and G_0W_0@scCOHSEX calculations are performed on the $20 \times 20 \times 1$ grid. The PBE and G_0W_0@PBE calculations are first performed on the $20 \times 20 \times 1$ grid and then interpolated to a finer 121-point k-path along the Y-Γ-Y line. The indirect band gaps measured on the coarse $20 \times 20 \times 1$ grid and the fine 121-point k-path are labeled accordingly.

Structure	Indirect band gap / eV						$E_{v_1} - E_{v_2}$ at Γ / eV			
Exp. [5]	0.055(20)						∼0.4 − 0.5			
	PBE		G_0W_0@PBE		scG_0W0	G_0W_0@scCOHSEX	PBE	G_0W_0@PBE	scG_0W_0	G_0W_0@scCOHSEX
	Coarse	Fine	Coarse	Fine						
[43]	−0.110		−0.070				0.399	0.498		
Relaxed	−0.066	−0.066	−0.010	−0.016	0.007	0.052	0.339	0.419	0.418	0.359
3% strain	0.062	0.055	0.321	0.308			0.180	0.210		

52 meV band gap calculated in the $20 \times 20 \times 1$ grid. The difference between the true band gap and the band gap on the $20 \times 20 \times 1$ coarse **k**-grid, however, is estimated to be $\lesssim 10$ meV by comparison of the conduction-band minima in the semimetallic G_0W_0@PBE band structure before and after Wannier interpolation, and we expect G_0W_0@scCOHSEX to maintain a positive band gap on a denser **k**-grid. Also, the distance between the highest two valence bands and the second highest two valence bands is slightly underestimated. Overall, the resulting band structure is close to the HSE06 band structure in Ref. [5] [Fig. 3(c)], which suggests that the exact exchange plays an important role in accurately describing the ground state of this system. We note that while we update the wave functions, the dielectric matrix is not updated and corresponds to the original semimetallic state. If the dielectric matrix is updated with the G_0W_0@scCOHSEX band structure, the indirect band gap increases dramatically to 191 meV, but there is no unphysical camelbacking. This is consistent with the previous observation that self-consistent *GW* without vertex corrections tends to overestimate the band gap [79].

V. POSSIBILITY OF EXCITON INSTABILITY

Finally, we investigate the stability of the three insulating ground states discussed in Secs. III and IV, namely (a) the PBE band structure from the 3%-strained and relaxed crystal structure, (b) the G_0W_0@PBE band structure from the 3%-strained and relaxed crystal structure, and (c) the G_0W_0@scCOHSEX band structure (Table II). In all three cases we perform a $\mathbf{Q} = \mathbf{0}$ BSE calculation and a finite-$\mathbf{Q}$ calculation. The finite momenta used in cases (b) and (c) are determined by minimizing the corresponding indirect band gap, which makes exciton instability more likely to happen. In case (c), we choose $\mathbf{Q} = (0, 0.15, 0)$ in crystal coordinates, which is comparable to the position of the exciton band minimum reported in [11], and in case (b) we choose $\mathbf{Q} = (0, 0.05, 0)$. For comparison of the exciton binding energy with case (b), in case (a) the $\mathbf{Q}$ used in the finite momentum calculation is also $(0, 0.05, 0)$.

In case (a), the DFT energy levels based on the strained structure is used, and the lowest-energy exciton calculated within BSE at both the direct and indirect gap has a negative excitation energy. The binding energy of the zero

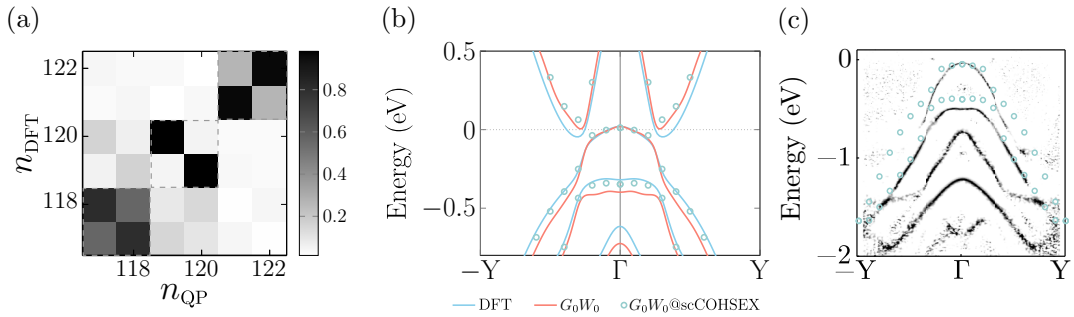

FIG. 3. Nondiagonal self-consistent calculations. (a) The overlap $|\langle\psi^{\mathrm{DFT}}_{n\mathbf{k}}|\psi^{\mathrm{QP}}_{n\mathbf{k}}\rangle|$ between the PBE Kohn-Sham wave functions and the wave functions corrected by scG_0W_0 at $\mathbf{k} = (0, 0.15, 0)$. $n_{\mathbf{QP}}$ and n_{DFT} refer to band indices after and before rediagonalization of the G_0W_0 Hamiltonian. Spin-degeneracy subspaces are marked by gray boxes. The number of occupied bands in the DFT calculation is 120, and band hybridization can be observed both within occupied states and between empty and occupied states. (b) Comparison between Fig. 2(c) and G_0W_0 corrections (green circles) on top of the scCOHSEX corrected wave functions. (c) G_0W_0@scCOHSEX (blue circles) compared with ARPES dispersion reproduced using a minimum gradient method [77] with data in Ref. [5] (used with permission). The valance-band top of the G_0W_0@scCOHSEX bands is manually aligned with the valence-band top of the ARPES spectrum. Note that the ARPES spectrum also has contributions from the Γ-P/P' directions, therefore the G_0W_0@scCOHSEX prediction of the highest valence band on the Γ-Y path deviates from the experimental ARPES spectrum away from Γ, although the experimental data around Γ are dominated by the Γ-Y path [cf. Fig. 2(g) in [5]].

TABLE II. Exciton energies in eV, based on 3%-strained and relaxed structure and the unstrained but G_0W_0@scCOHSEX-corrected electronic structure. The coarse grid refers to the grid on which the BSE kernel is calculated. The BSE kernel is then interpolated to the fine grid. E^{gap} refers to the direct/indirect independent-particle band gap, which always corresponds to the smallest direct gap on the fine **k**-grid used in each set of calculations. The binding energies are calculated from the difference between the direct (indirect) gap and the minimum exciton energy at zero momentum (finite momentum corresponding to the momentum transfer at the gap). The BSE@G_0W_0@scCOHSEX calculation is not fully converged, and the minimum exciton energies reported here are expected to be higher than the fully converged minimum exciton energies.

			Direct			Indirect		
Single-particle picture	Coarse grid	Fine grid	E^{gap} (eV)	min E^{ex} (eV)	E^{bind} (eV)	E^{gap} (eV)	min E^{ex} (eV)	E^{bind} (eV)
PBE, 3% strain	$20 \times 20 \times 1$	$200 \times 200 \times 1$	0.125	−0.115	0.240	0.065	−0.214	0.279
G_0W_0@PBE, 3% strain	$20 \times 20 \times 1$	$200 \times 200 \times 1$	0.359	0.137	0.222	0.318	0.045	0.273
G_0W_0@scCOHSEX@PBE	$20 \times 20 \times 1$	$20 \times 20 \times 1$	0.285	<0.182	∼ 0.103	0.052	< −0.082	∼0.134

center-of-mass momentum ($\mathbf{Q} = \mathbf{0}$) exciton is 240 meV while the binding energy of the indirect band-gap exciton is 279 meV. In comparison, the binding energy of the indirect exciton calculated by BSE on top of HSE, in Ref. [11], is 333 meV. In case (b), after the G_0W_0 correction, the lowest exciton excitation energies at both the indirect band gap and the direct band gap increase to positive values. This is because the exciton binding energy remains roughly the same after the *GW* renormalization of the band structure, and the magnitude of the *GW* correction is larger than the exciton binding energy. This contrasts with the behavior of other materials where negative exciton excitation energies at the BSE level are observed when the BSE calculation is performed on top of the *GW* band structure [25]. BSE calculations on other systems with suspected exciton instabilities also consistently show negative exciton energies before and after *GW* corrections [24,26].

Next, we turn to case (c), the G_0W_0@scCOHSEX calculation. Due to the computational cost of updating the wave function on a fine grid, our BSE calculation uses a $20 \times 20 \times 1$ coarse grid without interpolation to a fine grid. This unconverged calculation places a lower bound on the exciton binding energy, as further convergence increases the binding energy [Fig. 1(c)]. Additionally, we note that we use the updated *W* from the insulating ground state for our BSE calculation to more accurately reflect the insulating screening seen in experiment. Under these calculation conditions, we find that the lowest indirect band-gap exciton still has a negative excitation energy of −82 meV. Using a semimetallic screening from the PBE mean field results in a minimum exciton excitation energy of 22 meV, suggesting that the excitation energy may become negative with further convergence [Fig. 1(c)]. No negative exciton energy is seen when $\mathbf{Q} = \mathbf{0}$, but the exciton binding energy is comparable to that of the indirect band-gap exciton.

VI. CONCLUSION

We have presented a comprehensive analysis of various factors affecting the accuracy of *ab initio* calculations of the electronic structure and excitonic properties of monolayer $1T'$ WTe_2. Our results highlight the failure of the conventional PBE functional in describing the ground state. In particular, we show that $1T'$ WTe_2 is semimetallic in a carefully converged G_0W_0@PBE calculation. Structural distortions open the band gap but introduce unphysical renormalization of the band structure. We show that using QP wave functions by updating DFT wave functions within either a nondiagonal scG_0W_0 or scCOHSEX results in a semiconducting band structure that agrees qualitatively with previous ARPES measurements. The scCOHSEX results are also in excellent agreement with previous HSE calculations, highlighting the inadequacy of the PBE ground state and justifying the success of HSE in previous calculations on the material. Finally, our finite-momentum BSE calculations performed on top of the quasiparticle wave functions suggest that exciton instability in the form of excitons with negative excitation energies is likely present in monolayer $1T'$ WTe_2. This is consistent with the hypothesis that monolayer $1T'$ WTe_2 is an excitonic insulator. It should be noted, however, that other correlated states of matter due to excitonic instability are also possible, and thus an exciton mode with a negative energy is necessary but not sufficient evidence for an excitonic insulator phase [80].

ACKNOWLEDGMENTS

This work was primarily supported by the National Science Foundation (NSF) Condensed Matter and Materials Theory (CMMT) program under Award No. DMR-2337987, which supported the self-consistent COHSEX calculations, and the NSF CMMT under Award No. DMR-2114081, which supported the initial calculations on the strained structure. Development of the BerkeleyGW code was supported by Center for Computational Study of Excited-State Phenomena in Energy Materials (C2SEPEM) at the Lawrence Berkeley National Laboratory, funded by the U.S. Department of Energy, Office of Science, Basic Energy Sciences, Materials Sciences and Engineering Division, under Contract No. DE-AC02-05CH11231. The calculations used resources of the National Energy Research Scientific Computing (NERSC), a DOE Office of Science User Facility operated under Contract No. DE-AC02-05CH11231; and the Texas Advanced Computing Center (TACC) at The University of Texas at Austin. Y.H. acknowledge support by the National Science Foundation (NSF) under Award No. DMR-2239171. We thank Shujie Tang (Chinese Academy of Sciences) for providing us with the raw ARPES data, and Zhenglu Li (USC) for helpful discussions.

[1] Y. Wu, D. Mou, N. H. Jo, K. Sun, L. Huang, S. L. Bud'ko, P. C. Canfield, and A. Kaminski, Observation of Fermi arcs in the type-II Weyl semimetal candidate WTe_2, Phys. Rev. B **94**, 121113(R) (2016).

[2] P. Li, Y. Wen, X. He, Q. Zhang, C. Xia, Z.-M. Yu, S. A. Yang, Z. Zhu, H. N. Alshareef, and X.-X. Zhang, Evidence for topological type-II Weyl semimetal WTe_2, Nat. Commun. **8**, 2150 (2017).

[3] Q. Wang, J. Zheng, Y. He, J. Cao, X. Liu, M. Wang, J. Ma, J. Lai, H. Lu, S. Jia *et al.*, Robust edge photocurrent response on layered type-II Weyl semimetal WTe_2, Nat. Commun. **10**, 5736 (2019).

[4] B. Zhao, B. Karpiak, D. Khokhriakov, A. Johansson, A. M. Hoque, X. Xu, Y. Jiang, I. Mertig, and S. P. Dash, Unconventional charge–spin conversion in Weyl-semimetal WTe_2, Adv. Mater. **32**, 2000818 (2020).

[5] S. Tang, C. Zhang, D. Wong, Z. Pedramrazi, H.-Z. Tsai, C. Jia, B. Moritz, M. Claassen, H. Ryu, S. Kahn *et al.*, Quantum spin Hall state in monolayer $1T'$-WTe_2, Nat. Phys. **13**, 683 (2017).

[6] L. Peng, Y. Yuan, G. Li, X. Yang, J.-J. Xian, C.-J. Yi, Y.-G. Shi, and Y.-S. Fu, Observation of topological states residing at step edges of WTe_2, Nat. Commun. **8**, 659 (2017).

[7] Z. Fei, T. Palomaki, S. Wu, W. Zhao, X. Cai, B. Sun, P. Nguyen, J. Finney, X. Xu, and D. H. Cobden, Edge conduction in monolayer WTe_2, Nat. Phys. **13**, 677 (2017).

[8] Y. Shi, J. Kahn, B. Niu, Z. Fei, B. Sun, X. Cai, B. A. Francisco, D. Wu, Z.-X. Shen, X. Xu *et al.*, Imaging quantum spin Hall edges in monolayer WTe_2, Sci. Adv. **5**, eaat8799 (2019).

[9] P. Wang, G. Yu, Y. Jia, M. Onyszczak, F. A. Cevallos, S. Lei, S. Klemenz, K. Watanabe, T. Taniguchi, R. J. Cava *et al.*, Landau quantization and highly mobile fermions in an insulator, Nature (London) **589**, 225 (2021).

[10] Y. Jia, P. Wang, C.-L. Chiu, Z. Song, G. Yu, B. Jäck, S. Lei, S. Klemenz, F. A. Cevallos, M. Onyszczak *et al.*, Evidence for a monolayer excitonic insulator, Nat. Phys. **18**, 87 (2022).

[11] B. Sun, W. Zhao, T. Palomaki, Z. Fei, E. Runburg, P. Malinowski, X. Huang, J. Cenker, Y.-T. Cui, J.-H. Chu *et al.*, Evidence for equilibrium exciton condensation in monolayer WTe_2, Nat. Phys. **18**, 94 (2022).

[12] B. Halperin and T. Rice, Possible anomalies at a semimetal-semiconductor transistion, Rev. Mod. Phys. **40**, 755 (1968).

[13] V.-N. Phan, K. W. Becker, and H. Fehske, Spectral signatures of the BCS-BEC crossover in the excitonic insulator phase of the extended Falicov-Kimball model, Phys. Rev. B **81**, 205117 (2010).

[14] C. Chen, W. Tang, X. Chen, Z. Kang, S. Ding, K. Scott, S. Wang, Z. Li, J. P. Ruff, M. Hashimoto *et al.*, Anomalous excitonic phase diagram in band-gap-tuned $Ta_2Ni(Se, S)_5$, Nat. Commun. **14**, 7512 (2023).

[15] D. Jérome, T. Rice, and W. Kohn, Excitonic insulator, Phys. Rev. **158**, 462 (1967).

[16] J. Zittartz, Theory of the excitonic insulator in the presence of normal impurities, Phys. Rev. **164**, 575 (1967).

[17] Y. H. Kwan, T. Devakul, S. L. Sondhi, and S. A. Parameswaran, Theory of competing excitonic orders in insulating WTe_2 monolayers, Phys. Rev. B **104**, 125133 (2021).

[18] It should be noted that exciton instability may drive the ground state into other phases as well, so negative frequency excitations should be seen as indicating the *possibility* of an excitonic insulator ground state rather than as direct evidence [17,80].

[19] H. Cercellier, C. Monney, F. Clerc, C. Battaglia, L. Despont, M. G. Garnier, H. Beck, P. Aebi, L. Patthey, H. Berger *et al.*, Evidence for an excitonic insulator phase in $1T$-$TiSe_2$, Phys. Rev. Lett. **99**, 146403 (2007).

[20] L. Ma, P. X. Nguyen, Z. Wang, Y. Zeng, K. Watanabe, T. Taniguchi, A. H. MacDonald, K. F. Mak, and J. Shan, Strongly correlated excitonic insulator in atomic double layers, Nature (London) **598**, 585 (2021).

[21] P. X. Nguyen, L. Ma, R. Chaturvedi, K. Watanabe, T. Taniguchi, J. Shan, and K. F. Mak, Perfect Coulomb drag in a dipolar excitonic insulator, arXiv:2309.14940.

[22] Z. Wang, D. A. Rhodes, K. Watanabe, T. Taniguchi, J. C. Hone, J. Shan, and K. F. Mak, Evidence of high-temperature exciton condensation in two-dimensional atomic double layers, Nature (London) **574**, 76 (2019).

[23] D. Varsano, S. Sorella, D. Sangalli, M. Barborini, S. Corni, E. Molinari, and M. Rontani, Carbon nanotubes as excitonic insulators, Nat. Commun. **8**, 1461 (2017).

[24] Z. Jiang, Y. Li, W. Duan, and S. Zhang, Half-excitonic insulator: A single-spin Bose-Einstein condensate, Phys. Rev. Lett. **122**, 236402 (2019).

[25] D. Varsano, M. Palummo, E. Molinari, and M. Rontani, A monolayer transition-metal dichalcogenide as a topological excitonic insulator, Nat. Nanotechnol. **15**, 367 (2020).

[26] Z. Jiang, W. Lou, Y. Liu, Y. Li, H. Song, K. Chang, W. Duan, and S. Zhang, Spin-triplet excitonic insulator: The case of semi-hydrogenated graphene, Phys. Rev. Lett. **124**, 166401 (2020).

[27] L. Hedin, New method for calculating the one-particle Green's function with application to the electron-gas problem, Phys. Rev. **139**, A796 (1965).

[28] M. S. Hybertsen and S. G. Louie, Electron correlation in semiconductors and insulators: Band gaps and quasiparticle energies, Phys. Rev. B **34**, 5390 (1986).

[29] S. Albrecht, L. Reining, R. Del Sole, and G. Onida, *Ab initio* calculation of excitonic effects in the optical spectra of semiconductors, Phys. Rev. Lett. **80**, 4510 (1998).

[30] M. Rohlfing and S. G. Louie, Electron-hole excitations and optical spectra from first principles, Phys. Rev. B **62**, 4927 (2000).

[31] L. X. Benedict, E. L. Shirley, and R. B. Bohn, Optical absorption of insulators and the electron-hole interaction: An *ab initio* calculation, Phys. Rev. Lett. **80**, 4514 (1998).

[32] X. Blase, I. Duchemin, D. Jacquemin, and P.-F. Loos, The Bethe–Salpeter equation formalism: From physics to chemistry, J. Phys. Chem. Lett. **11**, 7371 (2020).

[33] W. Kohn and L. J. Sham, Self-consistent equations including exchange and correlation effects, Phys. Rev. **140**, A1133 (1965).

[34] J. P. Perdew and M. R. Norman, Electron removal energies in Kohn-Sham density-functional theory, Phys. Rev. B **26**, 5445 (1982).

[35] J. P. Perdew and M. Levy, Physical content of the exact Kohn-Sham Orbital energies: Band gaps and derivative discontinuities, Phys. Rev. Lett. **51**, 1884 (1983).

[36] M. Grüning, A. Marini, and A. Rubio, Density functionals from many-body perturbation theory: The band gap for semiconductors and insulators, J. Chem. Phys. **124**, 154108 (2006).

[37] S. Kümmel and L. Kronik, Orbital-dependent density functionals: Theory and applications, Rev. Mod. Phys. **80**, 3 (2008).

[38] J. P. Perdew, K. Burke, and M. Ernzerhof, Generalized gradient approximation made simple, Phys. Rev. Lett. **77**, 3865 (1996).

[39] A. Marrazzo, Thermal robustness of the quantum spin Hall phase in monolayer WTe_2, Phys. Rev. Mater. **7**, L021201 (2023).

[40] H. Lv, W. Lu, D. Shao, Y. Liu, S. Tan, and Y. Sun, Perfect charge compensation in WTe_2 for the extraordinary magnetoresistance: From bulk to monolayer, Europhys. Lett. **110**, 37004 (2015).

[41] H. Xiang, B. Xu, J. Liu, Y. Xia, H. Lu, J. Yin, and Z. Liu, Quantum spin Hall insulator phase in monolayer WTe_2 by uniaxial strain, AIP Adv. **6**, 095005 (2016).

[42] M. Grumet, P. Liu, M. Kaltak, J. Klimeš, and G. Kresse, Beyond the quasiparticle approximation: Fully self-consistent *GW* calculations, Phys. Rev. B **98**, 155143 (2018).

[43] X. Qian, J. Liu, L. Fu, and J. Li, Quantum spin Hall effect in two-dimensional transition metal dichalcogenides, Science **346**, 1344 (2014).

[44] J. Heyd, G. E. Scuseria, and M. Ernzerhof, Hybrid functionals based on a screened Coulomb potential, J. Chem. Phys. **118**, 8207 (2003).

[45] F. Zheng, C. Cai, S. Ge, X. Zhang, X. Liu, H. Lu, Y. Zhang, J. Qiu, T. Taniguchi, K. Watanabe *et al.*, On the quantum spin Hall gap of monolayer 1T′-WTe_2, Adv. Mater. **28**, 4845 (2016).

[46] I. Cucchi, I. Gutiérrez-Lezama, E. Cappelli, S. McKeown Walker, F. Y. Bruno, G. Tenasini, L. Wang, N. Ubrig, C. Barreteau, E. Giannini *et al.*, Microfocus laser–angle-resolved photoemission on encapsulated mono-, bi-, and few-layer 1T′-WTe_2, Nano Lett. **19**, 554 (2019).

[47] S.-Y. Xu, Q. Ma, H. Shen, V. Fatemi, S. Wu, T.-R. Chang, G. Chang, A. M. M. Valdivia, C.-K. Chan, Q. D. Gibson *et al.*, Electrically switchable Berry curvature dipole in the monolayer topological insulator WTe_2, Nat. Phys. **14**, 900 (2018).

[48] S. Ok, L. Muechler, D. Di Sante, G. Sangiovanni, R. Thomale, and T. Neupert, Custodial glide symmetry of quantum spin Hall edge modes in monolayer WTe_2, Phys. Rev. B **99**, 121105(R) (2019).

[49] H.-D. Saßnick and C. Cocchi, Electronic structure of cesium-based photocathode materials from density functional theory: Performance of PBE, SCAN, and HSE06 functionals, Electron. Struct. **3**, 027001 (2021).

[50] C. Attaccalite, M. Grüning, and A. Marini, Real-time approach to the optical properties of solids and nanostructures: Time-dependent Bethe-Salpeter equation, Phys. Rev. B **84**, 245110 (2011).

[51] W. Gao, W. Xia, X. Gao, and P. Zhang, Speeding up GW calculations to meet the challenge of large scale quasiparticle predictions, Sci. Rep. **6**, 36849 (2016).

[52] T. Kotani, M. van Schilfgaarde, and S. V. Faleev, Quasiparticle self-consistent *GW* method: A basis for the independent-particle approximation, Phys. Rev. B **76**, 165106 (2007).

[53] F. Tang, Z. Li, C. Zhang, S. G. Louie, R. Car, D. Y. Qiu, and X. Wu, Many-body effects in the x-ray absorption spectra of liquid water, Proc. Natl. Acad. Sci. USA **119**, e2201258119 (2022).

[54] P. Giannozzi, S. Baroni, N. Bonini, M. Calandra, R. Car, C. Cavazzoni, D. Ceresoli, G. L. Chiarotti, M. Cococcioni, I. Dabo *et al.*, Quantum espresso: a modular and open-source software project for quantum simulations of materials, J. Phys.: Condens. Matter **21**, 395502 (2009).

[55] P. Giannozzi, O. Andreussi, T. Brumme, O. Bunau, M. B. Nardelli, M. Calandra, R. Car, C. Cavazzoni, D. Ceresoli, M. Cococcioni *et al.*, Advanced capabilities for materials modelling with QUANTUM ESPRESSO, J. Phys.: Condens. Matter **29**, 465901 (2017).

[56] D. R. Hamann, Optimized norm-conserving Vanderbilt pseudopotentials, Phys. Rev. B **88**, 085117 (2013).

[57] M. Schlipf and F. Gygi, Optimization algorithm for the generation of ONCV pseudopotentials, Comput. Phys. Commun. **196**, 36 (2015).

[58] P. Scherpelz, M. Govoni, I. Hamada, and G. Galli, Implementation and validation of fully relativistic GW calculations: spin–orbit coupling in molecules, nanocrystals, and solids, J. Chem. Theory Comput. **12**, 3523 (2016).

[59] N. Marzari and D. Vanderbilt, Maximally localized generalized wannier functions for composite energy bands, Phys. Rev. B **56**, 12847 (1997).

[60] A. A. Soluyanov and D. Vanderbilt, Computing topological invariants without inversion symmetry, Phys. Rev. B **83**, 235401 (2011).

[61] N. Marzari, A. A. Mostofi, J. R. Yates, I. Souza, and D. Vanderbilt, Maximally localized Wannier functions: Theory and applications, Rev. Mod. Phys. **84**, 1419 (2012).

[62] G. Pizzi, V. Vitale, R. Arita, S. Blügel, F. Freimuth, G. Géranton, M. Gibertini, D. Gresch, C. Johnson, T. Koretsune *et al.*, Wannier90 as a community code: new features and applications, J. Phys.: Condens. Matter **32**, 165902 (2020).

[63] J. Deslippe, G. Samsonidze, D. A. Strubbe, M. Jain, M. L. Cohen, and S. G. Louie, BerkeleyGW: A massively parallel computer package for the calculation of the quasiparticle and optical properties of materials and nanostructures, Comput. Phys. Commun. **183**, 1269 (2012).

[64] A. Dal Corso, Pseudopotentials periodic table: From H to Pu, Comput. Mater. Sci. **95**, 337 (2014).

[65] B. A. Barker, *Electronic and Optical Properties of Solids with Strong Spin-orbit Coupling* (University of California Press, Berkeley, CA, 2018).

[66] B. A. Barker, J. Deslippe, J. Lischner, M. Jain, O. V. Yazyev, D. A. Strubbe, and S. G. Louie, Spinor *GW*/Bethe-Salpeter calculations in BerkeleyGW: Implementation, symmetries, benchmarking, and performance, Phys. Rev. B **106**, 115127 (2022).

[67] S. Ismail-Beigi, Truncation of periodic image interactions for confined systems, Phys. Rev. B **73**, 233103 (2006).

[68] M. Del Ben, F. H. da Jornada, A. Canning, N. Wichmann, K. Raman, R. Sasanka, C. Yang, S. G. Louie, and J. Deslippe, Large-scale GW calculations on pre-exascale HPC systems, Comput. Phys. Commun. **235**, 187 (2019).

[69] W. Gao, F. H. da Jornada, M. Del Ben, J. Deslippe, S. G. Louie, and J. R. Chelikowsky, Quasiparticle energies and optical excitations of 3C-SiC divacancy from *GW* and *GW* plus Bethe-Salpeter equation calculations, Phys. Rev. Mater. **6**, 036201 (2022).

[70] A. R. Altman, S. Kundu, and F. H. da Jornada, Mixed stochastic-deterministic approach for many-body perturbation theory calculations, Phys. Rev. Lett. **132**, 086401 (2024).

[71] D. Y. Qiu, T. Cao, and S. G. Louie, Nonanalyticity, valley quantum phases, and lightlike exciton dispersion in monolayer transition metal dichalcogenides: Theory and first-principles calculations, Phys. Rev. Lett. **115**, 176801 (2015).

[72] M. Rohlfing and S. G. Louie, Electron-hole excitations in semiconductors and insulators, Phys. Rev. Lett. **81**, 2312 (1998).

[73] D. Y. Qiu, F. H. da Jornada, and S. G. Louie, Screening and many-body effects in two-dimensional crystals: Monolayer MoS_2, Phys. Rev. B **93**, 235435 (2016).

[74] F. H. da Jornada, D. Y. Qiu, and S. G. Louie, Nonuniform sampling schemes of the Brillouin zone for many-electron perturbation-theory calculations in reduced dimensionality, Phys. Rev. B **95**, 035109 (2017).

[75] B. Hou, D. Wang, B. A. Barker, and D. Y. Qiu, Exchange-driven intermixing of bulk and topological surface states by chiral excitons in Bi_2Se_3, Phys. Rev. Lett. **130**, 216402 (2023).

[76] A. M. Alvertis, A. Champagne, M. Del Ben, F. H. da Jornada, D. Y. Qiu, M. R. Filip, and J. B. Neaton, Importance of nonuniform Brillouin zone sampling for *ab initio* Bethe-Salpeter equation calculations of exciton binding energies in crystalline solids, Phys. Rev. B **108**, 235117 (2023).

[77] Y. He, Y. Wang, and Z.-X. Shen, Visualizing dispersive features in 2D image via minimum gradient method, Rev. Sci. Instrum. **88**, 073903 (2017).

[78] A. Mar, S. Jobic, and J. A. Ibers, Metal-metal vs tellurium-tellurium bonding in WTe_2 and its ternary variants $TaIrTe_4$ and $NbIrTe_4$, J. Am. Chem. Soc. **114**, 8963 (1992).

[79] A. L. Kutepov, Electronic structure of Na, K, Si, and LiF from self-consistent solution of Hedin's equations including vertex corrections, Phys. Rev. B **94**, 155101 (2016).

[80] G. Sethi, M. Cuma, and F. Liu, Excitonic condensate in flat valence and conduction bands of opposite chirality, Phys. Rev. Lett. **130**, 186401 (2023).